CHAPTER 3

Enhanced photocatalytic efficiency of hydrothermally synthesized g-C3N4/NiO heterostructure for mineralization of malachite green dye

3.1 Introduction

Today, the contamination of the water stream is one of the critical problems of the world, mainly due to the growing population and disposal of wastes from the elaboration of textiles as well as chemical industries. A synthetic dying agent employed in these industries is a major responsible for pollution of the environment because it is non biodegradable and having great toxicity towards both flora and fauna. MG is a green-colored, tri-phenylmethane dye that is used in encompassing manner in food, leather, silk, textile industries as an additive and as a dying agent because of its disinfectant and antibacterial nature (Sarmah and Kumar, 2011; Crini et al., 2007; Cheng et al., 2008). However, since 1990s, it is found that MG and leucomalachite green (reduced form of malachite green) has carcinogenic, mutagenic, and genotoxic effects on living beings (Rao, 1995; Alderman and Clifton-Hadley, 1993). Henceforth it is required to develop some efficient techniques for the removal of such types of hazardous organic recalcitrant's from the water stream. Several methods are used for expulsion of toxic materials from wastewater like biological treatment (Wang et al., 2011), adsorption (Mittal, 2006) process, and heterogeneous semiconductor photocatalysis (Sayılkan et al., 2007; Chen et al., 2007; Pare et al., 2011; Liu et al., 2010; Prado and Costa, 2009). Among these methods, semiconductor heterogeneous photocatalysis is one of the efficient methods for degradation of harmful organic wastes into CO_2 and H_2O, and it may occur in the presence of sunlight, which is eco-friendly and renewable energy source (Prado and Costa, 2009; Lee et al., 2012). From last several decades, heterogeneous semiconductor photocatalyst like TiO_2, WO_3, CuO, ZnO, Cu_2S, SnO_2, and NiO have drawn the researchers attention because of their higher photocatalytic efficiency as well as stability, less toxicity, reusability, cost effective and mainly, due to high capability towards the

degradation of toxic organic wastes into harmless compounds, i.e., CO_2, H_2O (Altın and Sökmen, 2014; Zhang et al., 2017; Saravanan et al., 2013, 2016; Cui et al., 2014; Elango and Roopan, 2016; Malwal and Gopinath, 2015; Zhou et al., 2020). In the process of wastewater remediation, NiO also has been used as a good adsorbent and shows better adsorption efficiency in comparison to CuO, *Y*-Al_2O_3, and several other metal oxides towards the adsorption of organic dyes (Wei et al., 2014; Darwish et al., 2019; Ai and Zeng, 2013). The particle size and bandgap of the synthesized photocatalysts have a major role in their photocatalytic performance. Pure NiO displays the properties of p-type semiconductor material and having an extensive optical bandgap, which is responsible for the fast recombination of the photogenerated excitons, consequentially, it shows poor photocatalytic activity (Chen et al., 2007). To overcome on such problems, recently, an organic metal-free moiety n-type g-C_3N_4 semiconductor with a bandgap of 2.70 eV is a promising candidate because of its low cost, high performance, nontoxicity, and spectacular optical properties. NiO and g-C_3N_4 give a potent p-n junction, which enhances the photocatalytic performance of the heterostructure. During this process, the internal electric field of the heterostructure helps to achieve the proper bandgap, consequently, decrease the rate of recombination of photogenerated electron-holes. There are very few reports on the photocatalytic applications of the heterostructured g-C_3N_4/NiO nanocomposite (Fu et al., 2018; Baig et al., 2020). There are some other reports in which g-C_3N_4 used as a dopant with nickel based materials that displays an efficient photocatalytic performance (Peng et al., 2019). In the present article, we synthesized novel hexagonal shaped nano heterojunction of n-type g-C_3N_4 (10 wt%) with p-type semiconductor NiO through hydrothermal deposition route followed by the calcination process. The synthesized heterojunction of g-C_3N_4/NiO nanocomposite displays efficient

photocatalytic activity with much higher turnover frequency (TOF) than previous studies. As synthesized nanocomposites (g-C_3N_4/NiO) also facilitate efficient charge separation between photogenerated excitons, which makes it a superior nanocomposite for MG dye degradation. The mechanism for the superiority of our synthesized catalyst could be endorsed with the proper optical band gap and fine internal transfer of charge carriers within the p-n junction in the presence of UV light.

3.2 Experimental

3.2.1 Synthesis of g-C_3N_4

g-C_3N_4 (SK-1) was synthesized by the thermal condensation method by using melamine as a precursor. 10 g of melamine was placed in an alumina crucible and put it into a muffle furnace at 550 °C temperature for 4 h with a ramp rate of 10 °C per minute (Li et al., 2013; Wu et al., 2019). The obtained yellow color material was further washed numerous times with ethyl alcohol and double distilled water to remove the impurities from the precipitate. Finally, g-C_3N_4 was collected by the centrifugation method and placed for drying into a vacuum oven at 60 °C.

3.2.2 Synthesis protocol of g-C_3N_4/NiO nanocomposite

g-C_3N_4 (195 mg) was redispersed in 30 mL ethyl alcohol, followed by sonication for 1 h. Hereafter, 0.22 M of $Ni(NO_3)_2.6H_2O$ was mixed with vigorous stirring. At that time, a 0.4 M sodium citrate solution was also added to the reaction mixture. Then, the mixed solution was allowed to transfer into the autoclave and placed into the oven for 12 h at 180 °C. After that, the autoclave was further cooled at room temperature. The obtained sample was centrifuged and washed properly with ethyl alcohol and double-distilled water to fix the impurities from the sample. The resulting nanocomposites were desiccated in a vacuum oven at 65 °C. The

nanocomposite was further transferred into an uncovered crucible of alumina and calcined in a muffle furnace at 500 °C temperature for 3 h. The found g-C_3N_4/NiO (SK-3) heterostructure nanocomposite was grinded for 5 min.; similar protocols were followed for the synthesis of pure NiO (SK-2) nanoparticle without using g-C_3N_4 (figure 3.1).

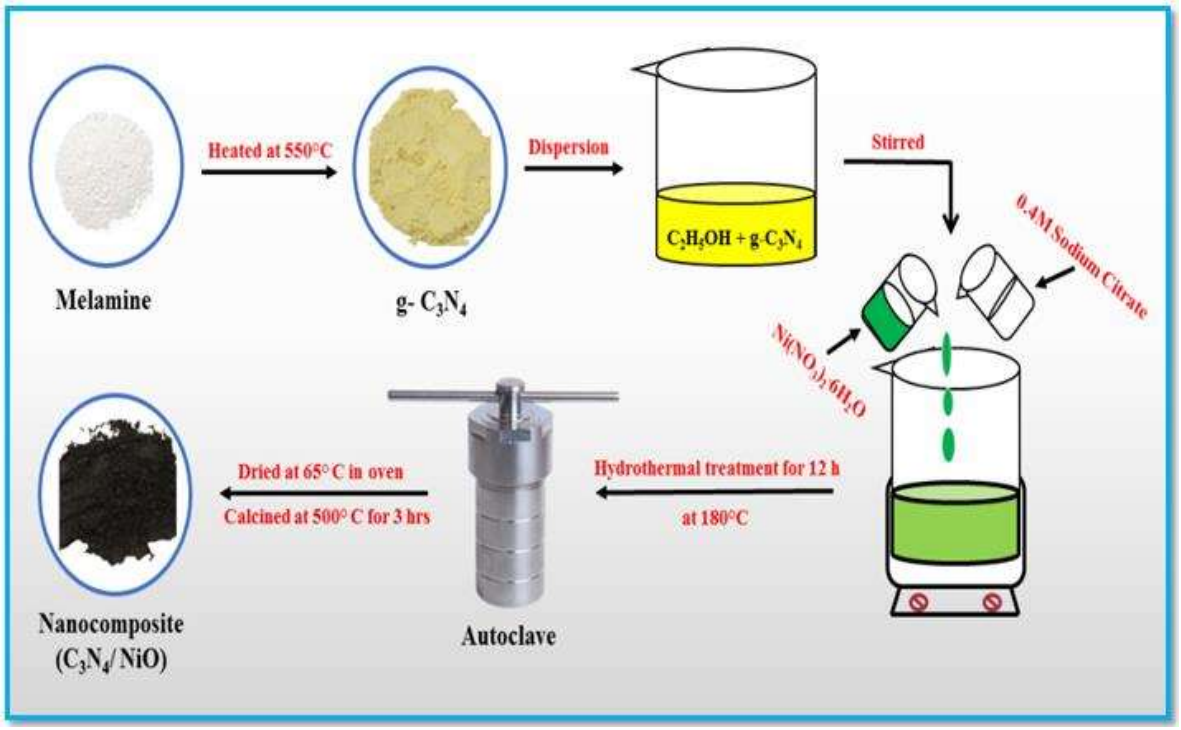

Fig. 3.1 The pictorial representation for the synthesis of SK-3 nanocomposite.

3.3 Characterization

As prepared samples were characterized by different characterization techniques discussed in section 2.4 of chapter 2.

3.3.1 Photocatalytic efficiency

Photocatalytic efficiency of g-C_3N_4 (SK-1) pure NiO (SK-2) and g-C_3N_4/NiO (SK-3) were explored through the photocatalytic mineralization of MG under UV light irradiation (254 nm, Phillips, 8 W). 10 mg of catalysts were redispersed in 100 mL aqueous solution of MG (2.76×10^{-5} mol/L) dye, and then the reaction mixture was further irradiated by UV light

(light source). The whole reaction was performed in a 1 cm path length quartz cuvette and recorded by the UV-Vis spectrophotometer. The change of the absorbance MG dye with the time indicates the degradation process of MG. The percentage degradation of MG was investigated by using following equation (Zhang et al., 2014).

$$\%\,\boldsymbol{Degradation} = \frac{A_0 - A_t}{A_0} \times 100 = \frac{C_0 - C_t}{C_0} \times 100 \qquad (3.1)$$

In the above equation A_0 and A_t is the initial and final absorbance (at 617 nm wavelength) of MG respectively while C_0 represents the initial concentration and C_t shows the MG concentration after the degradation.

3.4 Results and Discussion

3.4.1 HR-XRD

HR-XRD patterns of the prepared sample (SK-1, SK-2, and SK-3) are shown in figure 3.2a. SK-1 (g-C_3N_4) recorded two broad peaks at 2θ values 13.07° and 27.47°,which is indexed at [100] and [002] plane respectively (Joint Committee on Powder Difraction Standards (JCPDS) no. 87-1526). Broad peaks are an indicator of the poor crystallinity and small thickness of the samples. NiO (SK-2) shows sharp peaks at 2θ values 37.19°, 43.32°, 62.84°, 75.31°, and 79.35° are obtained (JCPDS Card no.04-0835) corresponding to the cubic crystal planes [111], [200], [220], [311], and [222] respectively. Here sharpness of peak visualizes the crystallinity of the sample. The formation of the Heterostructure of NiO with g-C_3N_4 (10 wt. %) is confirmed by the presence of the peaks for both NiO and g-C_3N_4 in g-C_3N_4/NiO (SK-3) nanocomposites. Figure 3.2 c and d represents the crystal structure of g-C_3N_4 (SK-1) and NiO (SK-2) respectively.

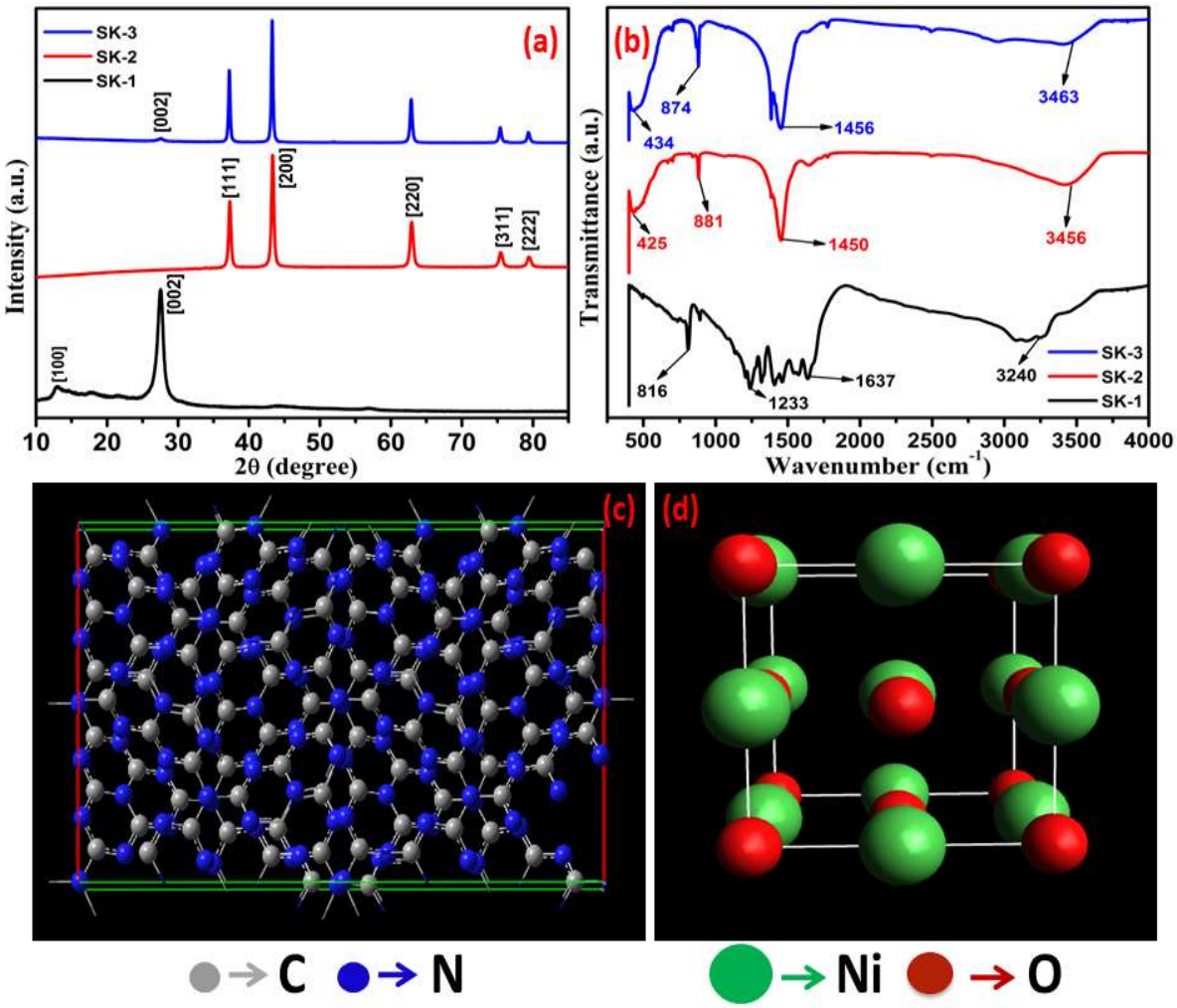

Fig. 3.2 (a) HR-XRD Pattern of SK-1, SK-2, and SK-3 (b) FT-IR spectra of SK-1, SK-2, And SK-3 samples, (c, d) Crystal structures of SK-1 and SK-2 respectively

3.4.2 FT-IR analysis

The samples were characterized through FT-IR for the functional group analysis and the type of vibrations present in the molecules, the result is displayed in figure 3.2b. In the case of SK-1 appearance of intense band at 1200-1650 cm^{-1} is mainly due to the aromatic stretching of C-N and C=N heterocycles. Apart from that, the vibration band at 816 cm^{-1} is due to the bending frequency of triazine rings (Shi et al., 2014; Lin et al., 2016). In the case of the SK-2 sample, at 425 cm^{-1}, a broad vibration band is recorded, which is responsible for the

stretching vibration between the Ni-O bonds (Selvarajan et al., 2018). All the band of SK-2 are also recorded in the case of SK-3, but the absorption band appear at 425 cm^{-1} in SK-2 is slightly shift at 434 cm^{-1}, which shows the interaction of the triazine ring of g-C_3N_4 with NiO by electrostatic interaction (Selvarajan et al., 2018). The absorption band around 1450 cm^{-1} is due to carbonate, and the band area at 3200-3500 cm^{-1} is corresponding to the vibrational stretching frequency of the O-H bond, which comes out due to unavoidable moisture absorbed by the sample from the atmosphere (Baig et al., 2020).

3.4.3 Morphology measurements

3.4.3.1 TEM and FE-SEM

The morphological properties of the nanoparticles were determined by TEM micrographs. Figure 3.3a demonstrates that most of the particles of SK-2 are spherical nanodiscs type with an average size is approx 35-40 nm (figure 3.3c). The corresponding SAED pattern shows the polycrystalline nature of SK-2, inset in figure 3.3a. The TEM micrograph of SK-3 (figure 3.3b) displays the hexagonal nanostructure of NiO is decorated with a g-C_3N_4 lamellar structure. For this, the SAED pattern is given in the inset of figure 3.3b, which indicates the crystalline properties of the composite because of the higher amount of the NiO component. The average diameter for heterostructure is shown in the histogram of figure 3.3d, which is found to be 25-30 nm. HR-TEM image of SK-3 is also given in the figure 3.3e; which validate the formation of the heterostructured nanocomposite. The particle size of composites is in good agreement with the XRD's crystallite size, which was calculated with the help of Scherer's equation. The SAED and XRD result is also very close to each other, and confirm the formation of SK-3 heterostructure through our designed scheme for its synthesis.

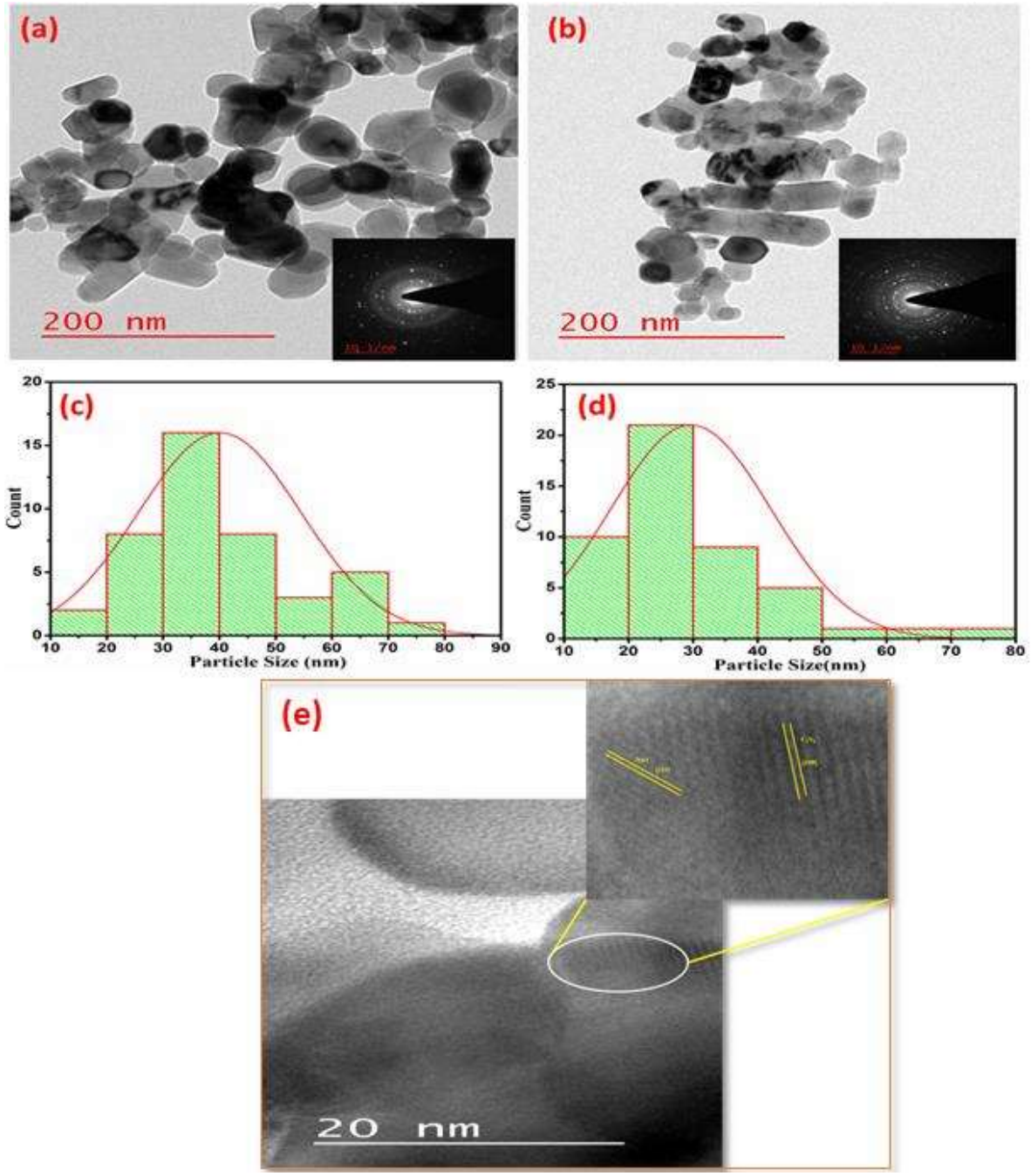

Fig. 3.3 TEM images of (a) SK-2, (b) SK-3 and SAED (inset), (c) histogram of the average size of SK-2, (d) the average size of SK-3, (e) HR-TEM image of SK-3

Figure 3.4a displays the FE-SEM image of SK-2, which depicts that the particles are slightly spherical, having small pores on its surface. The surface morphology and EDS spectrum of

SK-3 is displayed in figure 3.4b, c, from the figure, it is seen that spherical nanoparticles of NiO with a diameter between 25-35 nm are placed on the sheet-like surface of g-C_3N_4. Just like pure NiO, many tiny pores also exist on the surface of SK-3, which provides space for adsorption of MG. The EDS spectrum confirms the presence of all the elements present in SK-3.

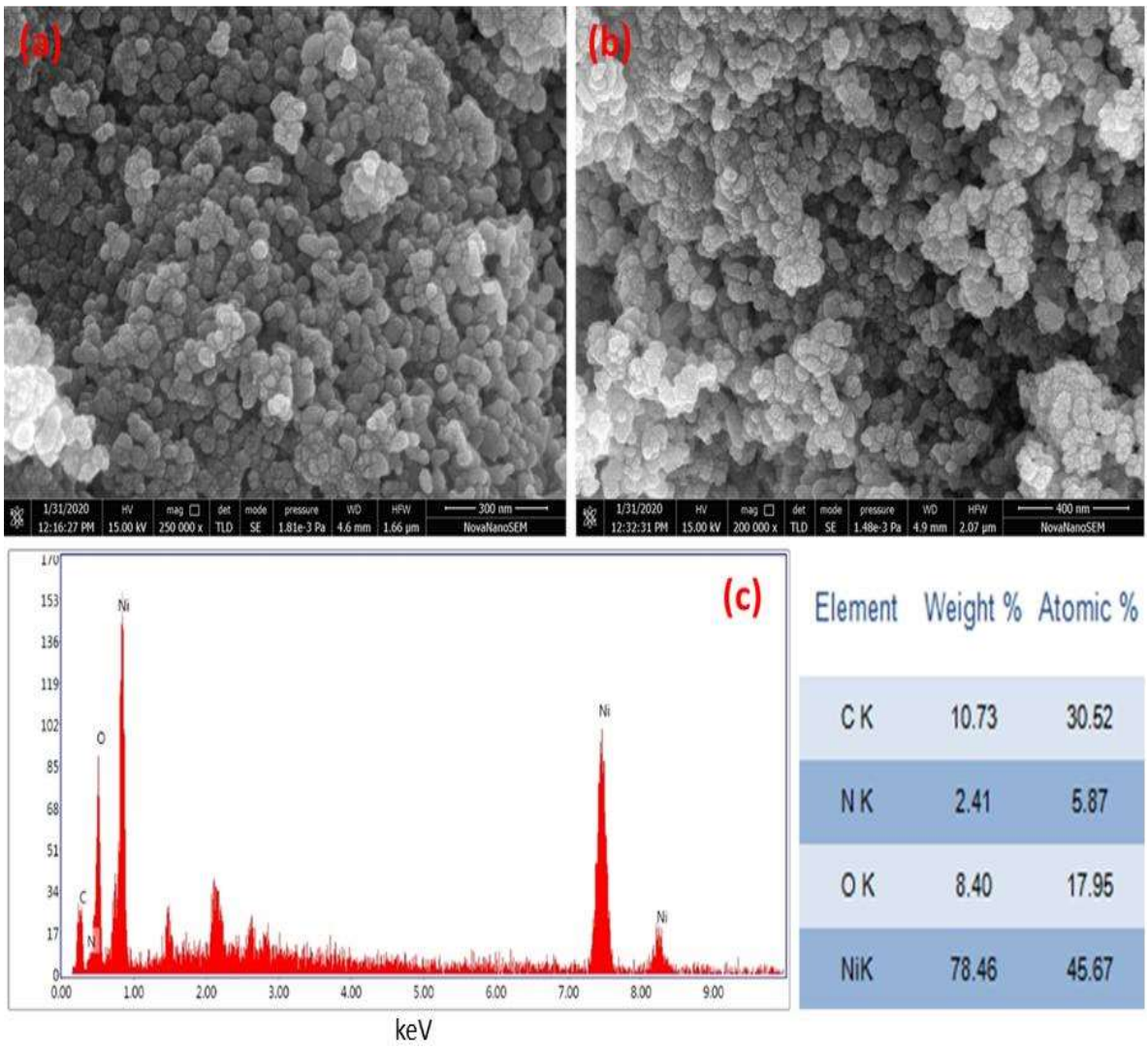

Fig. 3.4 FE-SEM images of (a) SK-2, (b) SK-3, and (c) EDS image of SK-3

3.4.3.2 B.E.T

The mesoporosity and specific surface area of the synthesized samples (SK-2 and SK-3)

were analyzed by N_2 adsorption-desorption isotherm and BET. The results of N_2 adsorption-desorption are provided in figure 3.5a and b which clearly shows hysteresis loops of type IV pattern that confirms the mesoporous nature of SK-2 and SK-3. The specific surface area was calculated with the help of the BET equation and it was 14 m^2/g and 22 m^2/g in SK-2 and SK-3 sample respectively. The pore diameter of the synthesized sample SK-3 is obtained arround 40-50 nm while in SK-2 sample the pore is of irregular diameter. Inset of figure 3.5a and b, which was determined by using Barret-Joyner-Halenda (BJH) plot (Labani et al., 2013).

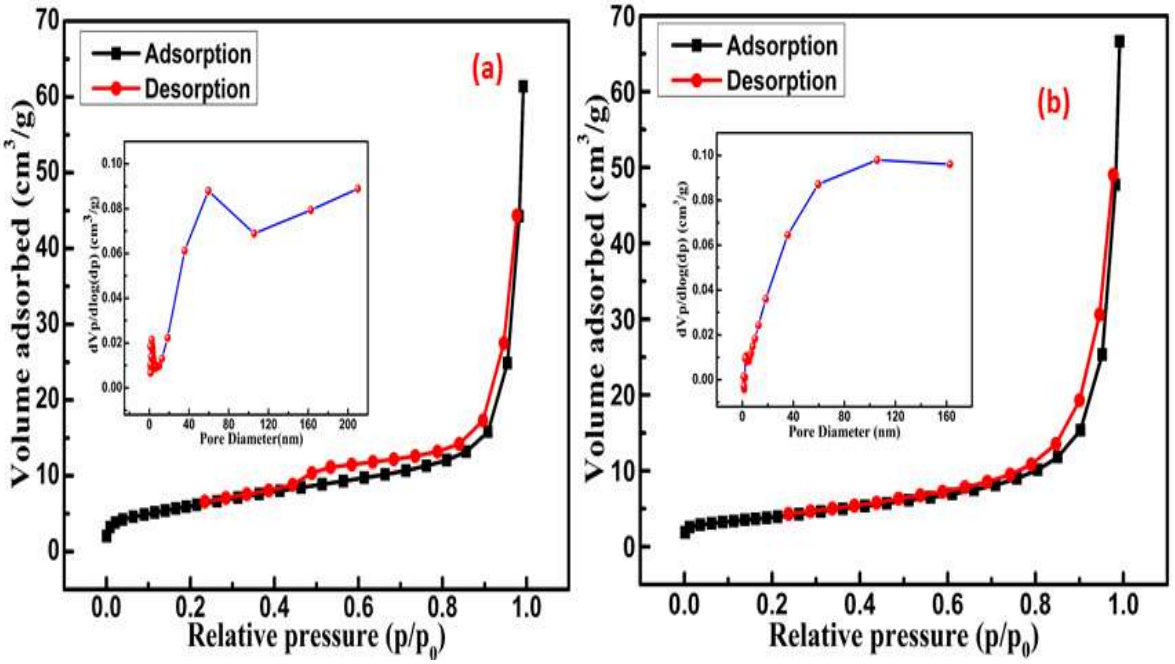

Fig. 3.5 N_2 adsorption-desorption isotherm and BJH plot (inset) for (a) SK-3, and (b) SK-2

3.4.4 X-ray photoelectron spectroscopy (XPS) analysis

The chemical composition and elemental states of the SK-3 heterostructure are analyzed by utilizing the principle of XPS. Figure 3.6 represents the XPS spectrum of the SK-3 sample. The heterostructured nanocomposite contains the following elements: C (photoelectrons from 1s), N (1s), O (1s), and Ni (2p). As shown in figure 3.6a The peaks at 284.5 eV correspond to

the C-C bond, whereas the peaks at 286.1 and 288.1 eV are because of the presence of sp^2 and sp^3 carbon of C=N and C-N bond, respectively in the g-C_3N_4 (Li et al., 2009; W. Zhang et al., 2016). Figure 3.6b displays the 1s spectra of nitrogen for SK-3 in which the peak at 398.7 eV attribute to sp^2 N (aromatic) attached with carbon (C=N-C) (Zhang et al., 2013) and the peaks at 399.2 and 401.2 eV correspond to N-$(C)_3$ groups, and due to pi excitations respectively (Thaweesak et al., 2017); In figure 3.6c the prominent peak at 528.6 and 529.1 eV are appeared because of the Ni-O bond, whereas the abundant peak at 531.7 eV attributed to the presence of the O species in water adsorbed on the surface (Santos et al., 2010; Guo et al., 2010; Y. Zhang et al., 2016). From figure 3.6d, the peak at 853.7 eV is due to Ni in $2p_{3/2}$, and the peak appeared at 879.1 eV, represent the $2p_{1/2}$ state of Ni, which confirms that Ni of NiO exists in +2 oxidation states (Y. Zhang et al., 2016). Other peaks present at 860.8 and 870.6 eV are satellite peaks that are induced by shake-up (Dai et al., 2014). The peak of Ni $2p_{3/2}$ at 855.4 eV and 1s peak of the O at 533.3 eV suggests the presence of Ni_2O_3 (figure 3.6d) (Kim and Davis, 1972).

Moreover, a slight variation in the binding energies of C 1s, O 1s, and Ni 2p are observed in the spectra of nanostructure composite (Huang et al., 2015; Lu et al., 2014) because of shifting of binding energy mainly due to variation in the electron concentration, which is happened due to transfer of electron and because of the interfacial interaction between p-n heterojunction. The spectrum of XPS survey of SK-3 also confirms the presence of all the above mentioned (i.e., C 1s, O 1s, N 1s, and Ni 2p) elements (figure 3.6e). Here, the +2 oxidation state of nickel helps in the modification of electron density corresponding to p-n junction and in the refinement of crystallinity of the nanocomposite. It also facilitates the charge separation, which is remarkable in the enhancement of photocatalytic activity.

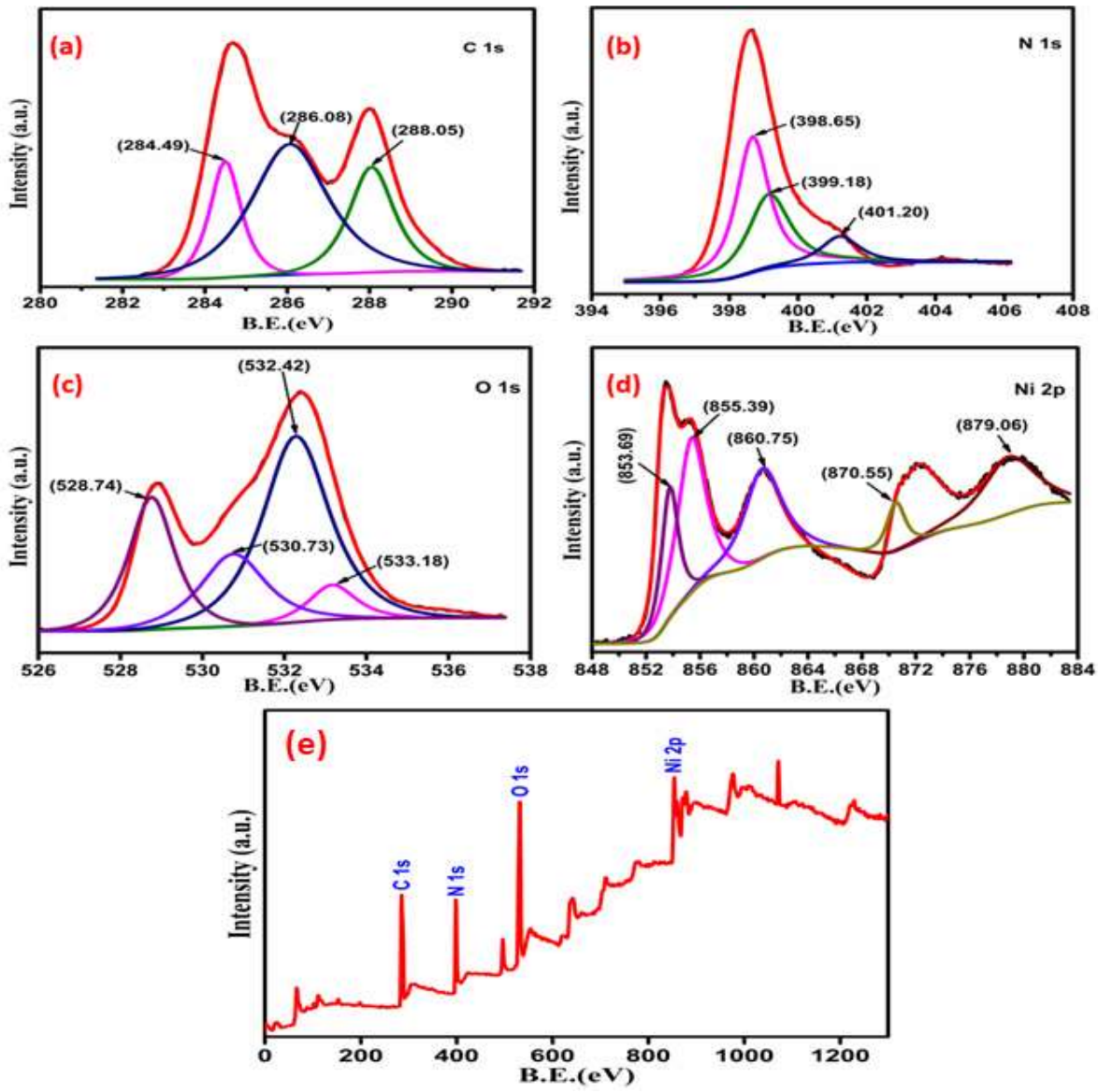

Fig. 3.6 XPS spectra of SK-3 sample for (a) Carbon 1s, (b) Nitrogen 1s, (c) Oxygen 1s, (d) Nickel 2p, and (e) XPS survey of SK-3 (Note: labeled peaks in figure a-d were obtained from XPS PEAK 41 software)

3.4.5 Optical property analysis

Bandgap calculation is essential to explain the photocatalytic mechanism. The absorbance data obtained from UV-Vis DRS are castoff to construct the Tauc plot for SK-1, SK-2, and SK-3 sample. Figure 3.7 shows the Tauc plots, which are drawn by using (Zhang et al., 2015;

Jahurul Islam et al., 2016; Yang et al., 2016; Wang et al., 2016; Xu and Schoonen, 2000).

$$(\alpha h\nu)^{1/n} = (h\nu - E_g) \qquad (3.2)$$

Where the symbol α denotes the molar absorption coefficient, photonic energy is represented by hν, and n = ½ value used for the direct transition (Zhang et al., 2015; Jahurul Islam et al., 2016). E_g signifies the optical bandgap energy of the materials. With the help of equation (3.2) the band gaps of pure SK-1, pure SK-2, and SK-3 nanocomposites were calculated as 2.63 eV, 3.30 eV, and 2.89 eV respectively.

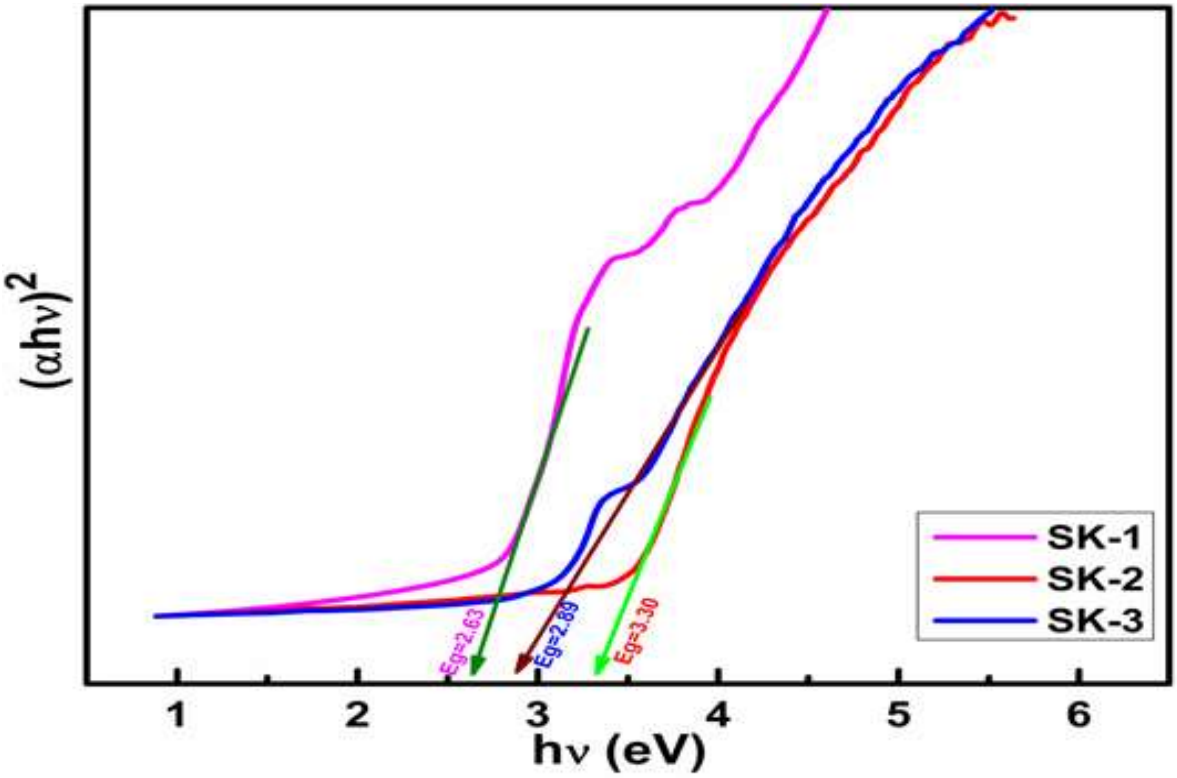

Fig. 3.7 Tauc plot of SK-1, SK-2, and SK-3

3.4.6 Photocatalytic degradation measurements

The results of the photocatalytic removal of MG under UV light over the porous surface of SK-3 nanocomposites are displayed in figure 3.8a. The MG displays a characteristic absorption peak at 617 nm; this was used as a signature to determine the degradation of MG.

This peak disappeared (96%) on irradiation for 12 min. There was no substantive change in the result beyond 12 min.

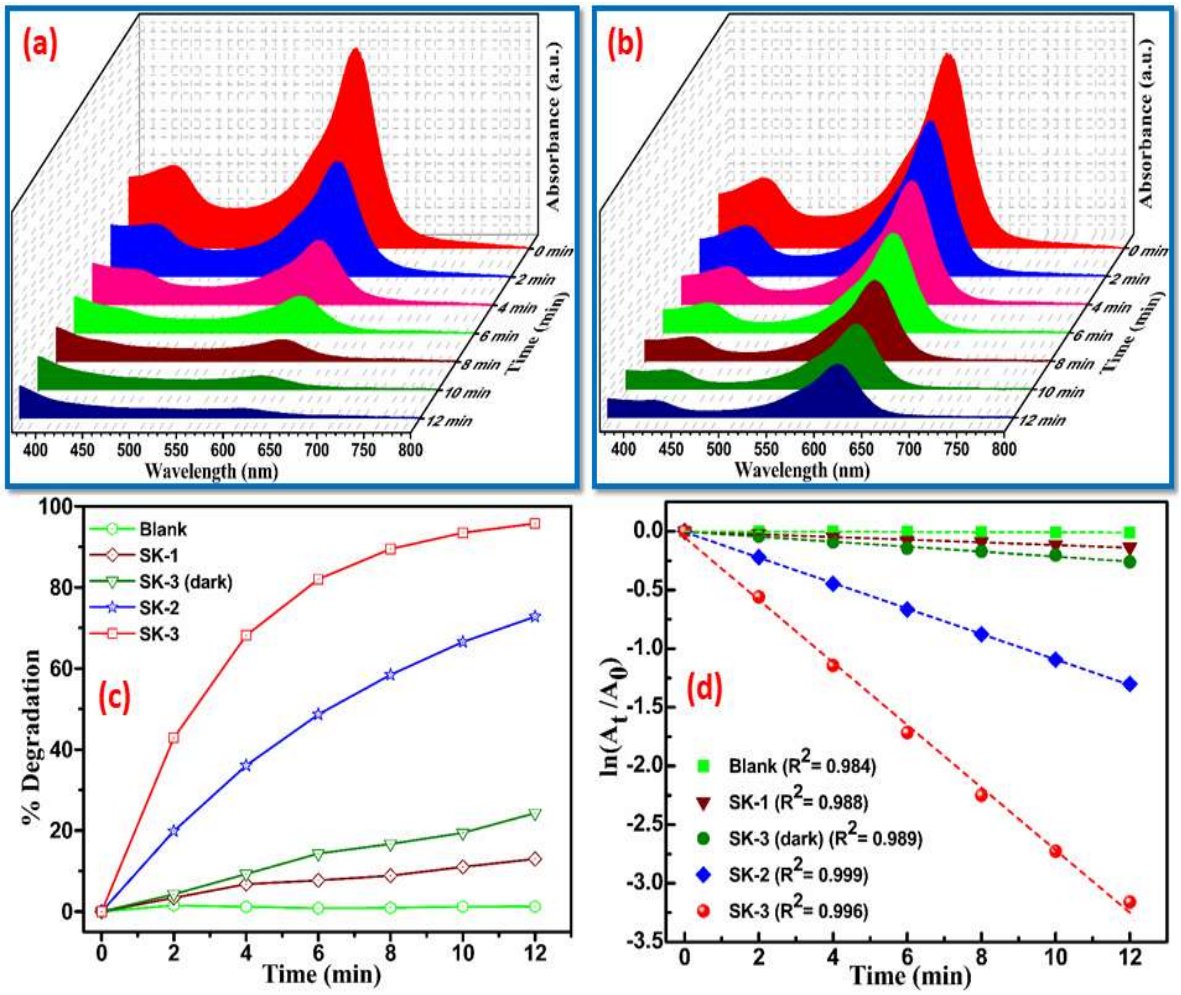

Fig. 3.8 UV-Visible Absorbance spectra of MG degradation by the photocatalyst (a) SK-3, (b) SK-2, (c) percentage degradation of MG with catalysts, and (d) kinetic plot for Blank, SK-1, SK-2 and SK-3 photocatalyst.

So, we have taken 12 min as a standard time for all other samples. Figure 3.8b displays the degradation of MG by SK-2, which was 72% at a similar time of 12 min. The efficiency of MG degradation by the different catalyst is displayed in figure 3.8c. The photolysis of MG is almost negligible in a blank experiment while SK-1 removes only 12% of MG dye (As

displays in figure 3.9a and b). The porous surface of SK-3 adsorbs about 23% MG under the dark condition, as it is well known that higher adsorption favors the photocatalysis. The photodegradation efficiency of MG over SK-3 achieves 96% in 12 min under UV light irradiation, which is greater than the SK-2 (72%) and SK-1 (12%). The reason for the higher photocatalytic efficiency of SK-3 is the formation of a p-n junction in between g-C_3N_4 and NiO, which facilitates the transfer of photogenerated excitons (e^-/h^+) and avoid the charge recombination process. The rate constants for photocatalytic degradation were calculated with the help of (Ma et al., 2011).

$$ln\left(\frac{A_0}{A_t}\right) = kt \qquad (3.3)$$

Here k represents the rate constant for dye degradation and t denotes the irradiation time of UV light. The rate constant of the reaction was determined by a slope that is obtained by plotting a kinetic graph between concentration $\ln\left(\frac{A_0}{A_t}\right)$ and t (time in min) as displays in figure 3.8d.

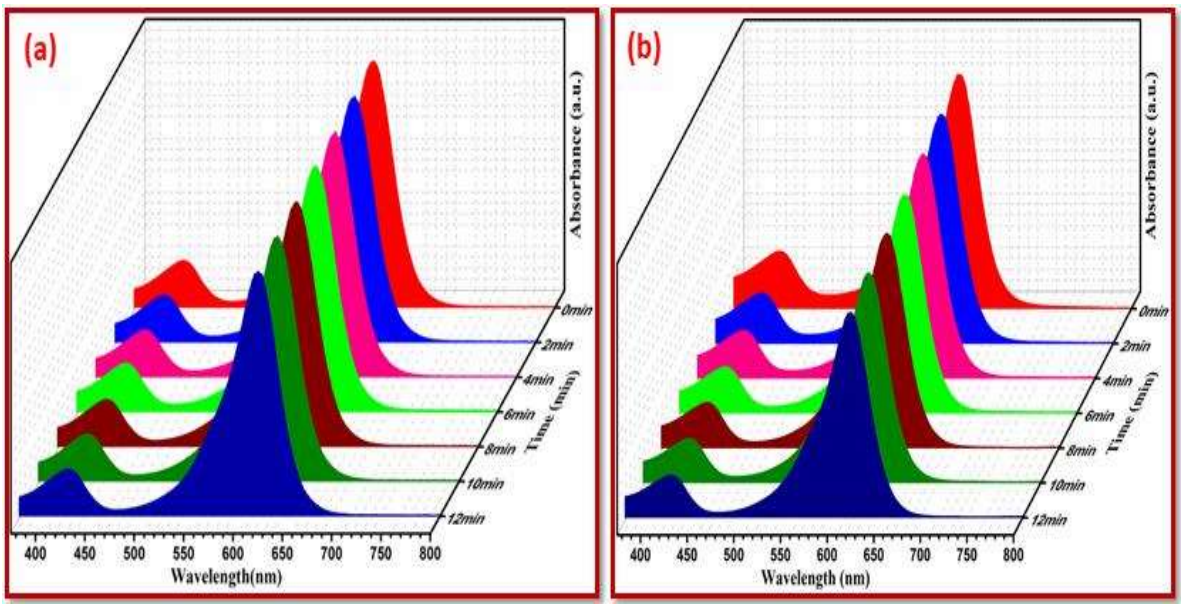

Fig. 3.9 MG degradation (a) blank, (b) MG degradation by SK-1 photocatalyst

The linear fitting of plots confirms the photocatalytic removal of MG is according to pseudo 1st order kinetics. The rate constant (k) and linearity coefficient (R^2) of SK-1, SK-2, and SK-3 obtained from kinetic plots are given in Table 3.1; which demonstrates that SK-3 has a higher value of degradation rate constant (k) as well as percentage degradation than that of SK-1 and SK-2, which validates that SK-3 is an efficient photocatalyst for the degradation of MG. Based on the above results, we can say that the loading of g-C_3N_4 (10 wt.%) with NiO performs the higher photocatalytic efficiency because of the formation of a strong p-n heterojunction, which delayed or avoid the recombination of photogenerated excitons (e^-/h^+). Simultaneously, low activity in SK-1 and SK-2 may be attributed due to poor charge transport and fast recombination of charge carriers (e^-/h^+).

Table 3.1 Representing the optical band gap, R^2, and rate constant (k) of SK-1, SK-2 and SK-3

Samples	Bandgap (eV)	Degradation (%) in 12 min.	R^2	Rate constant (min^{-1})
SK-1	2.63	12	0.988	1.14×10^{-2}
SK-2	3.30	72	0.999	1.08×10^{-1}
SK-3	2.89	96	0.996	2.66×10^{-1}

3.4.6.1 Effect of g-C_3N_4 content

In order to elucidate the impact of g-C_3N_4 content on the photocatalytic efficiency of SK-3 nanocomposite photocatalysts, a series of parallel experiments run to check the photocatalytic degradation of MG dye. The results of the MG degradation with SK-2 and NiO with 5 wt% (SK-3′), 10 wt% (SK-3), and 15 wt% (SK-3″) of g-C_3N_4 displayed in figure

3.10a. From the figure it is clear that the performance of the 10 wt% g-C_3N_4 is significantly higher than 5 and 15 wt% of g-C_3N_4 while the pure NiO has the lowest photocatalytic activity. The results indicate that there is an improvement in the photocatalytic performance in comparison with pure NiO. Figure 3.10a also reveals that when the g-C_3N_4 content is low, then the charge separation is insufficient; hence the photocatalytic activity of SK-3′ is slower than that of SK-3. However, on increasing the content of the g-C_3N_4 from 10 wt%, we found that the photocatalytic performance of the nanocomposite decreased because overloading of the g-C_3N_4 caused a shielding effect on the NiO and inhibited the contact between NiO and reactant MG.

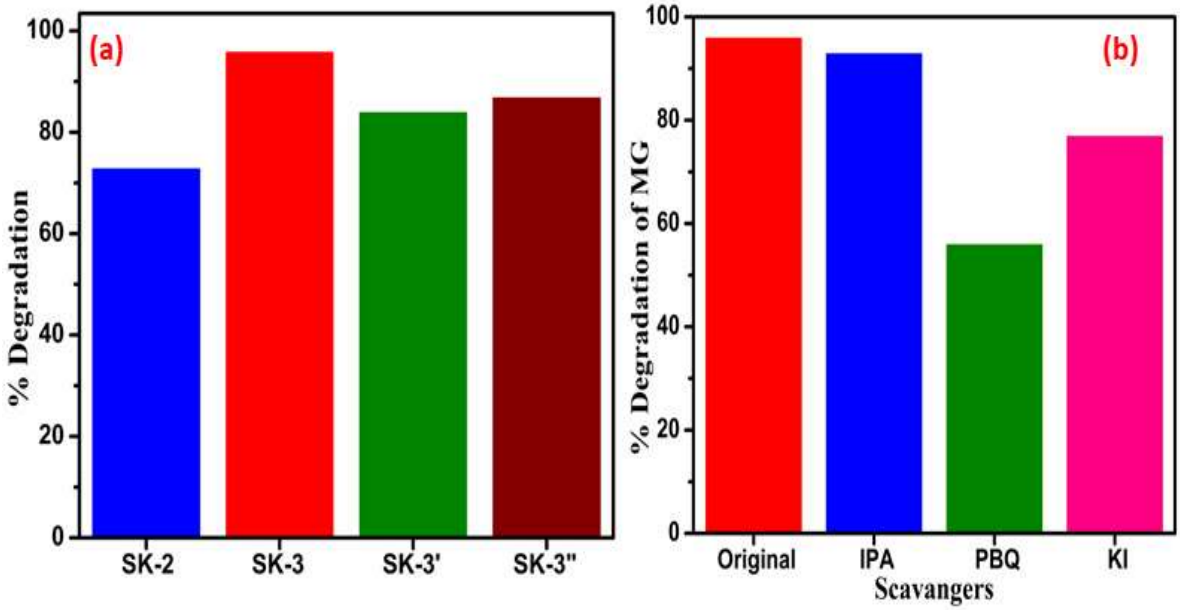

Fig. 3.10 (a) Effect of 5 wt% (SK-3′), 10 wt% (SK-3), and 15 wt% (SK-3″) of g-C_3N_4 content on MG degradation, (b) Effect of trapping agent on MG degradation (here PBQ molecule used to trap $O_2^{\bullet-}$ radicals, IPA as $OH^{\bullet}$ radical scavenger KI molecules used as h^+ scavenger)

3.4.6.2 Observation of active species involved in MG degradation

We have performed radical (active species) trapping experiments with SK-3 photocatalyst to

understand the chief reactive species formed during the photocatalytic removal of MG. The para-benzoquinone (PBQ) molecule used to trap $O_2^{\bullet-}$ radicals, iso-propyl alcohol (IPA) as $OH^{\bullet}$ radical scavenger, and potassium iodide (KI) molecules used as a hole (h^+) scavenger. The results of the radical trapping experiments displayed in figure 3.10b reveals that the photocatalytic removal of MG in the presence of PBQ was greatly inhibited in comparison to other scavengers. It confirms that superoxide radicals ($O_2^{\bullet-}$) are the main active species produced during the process of photocatalysis. KI (h^+ scavenger) also suppress the MG degradation, but the effect is less than PBQ and higher to IPA. So, $O_2^{\bullet-} > h^+ > OH^{\bullet}$ is the priority order of the active species generated during the photocatalytic reaction.

3.4.6.3 Mechanism of photocatalytic degradation of MG

The reason for the higher photocatalytic activity of SK-3 can be elucidated by a mechanism shown in figure 3.11, which displays the mode of electron transfer and the alignment of band positions of SK-3. Equation 3.4 and 3.5 was used to calculate the value of the conduction band (CB) and valence band (VB) edges, respectively (Zhang et al., 2015; Jahurul Islam et al., 2016; Yang et al., 2016).

$$\boldsymbol{E_{CB} = \chi - E^e - 0.5E_g} \qquad (3.4)$$

$$\boldsymbol{E_{VB} = \chi - E^e + 0.5E_g} \qquad (3.5)$$

In the above equations, χ (Chi) denotes the electronegativity; the energy of free electron on hydrogen scale represented by E^e and E_g shows the optical bandgap of heterostructure material. The E^e value is Constant i.e. (E^e = 4.5 eV). Valance band (VB = 1.55 eV) and conduction band (CB = -1.09 eV) of g-C_3N_4 is lying above than those of NiO (VB = 2.4 eV, CB = -0.4 eV), which facilitate the transfer of charge carrier (e^- and h^+). As shown from the band position of the SK-3 heterojunction nanocomposite behaves like a typical type-II

heterojunction photocatalyst. However, if charge transfer takes place according to type-II, then the transfer of electrons will take from CB of g-C_3N_4 to the CB of NiO and holes from the VB of NiO to the VB of g-C_3N_4, which may not have high reduction potential (only -0.40 eV for CB of NiO) and oxidation potential (only 1.55 eV for VB of g-C_3N_4) for generating $O_2^{\bullet-}$ radicals (-0.33 eV) and $OH^{\bullet}$ (2.40 eV). From the staggered band structure of the nanocomposite SK-3 and other experimental results, the most appropriate photocatalytic mechanism of charge transfer in SK-3 photocatalyst follows the step scheme (S-scheme) mechanism (Van Viet et al., 2022; Fu et al., 2019).

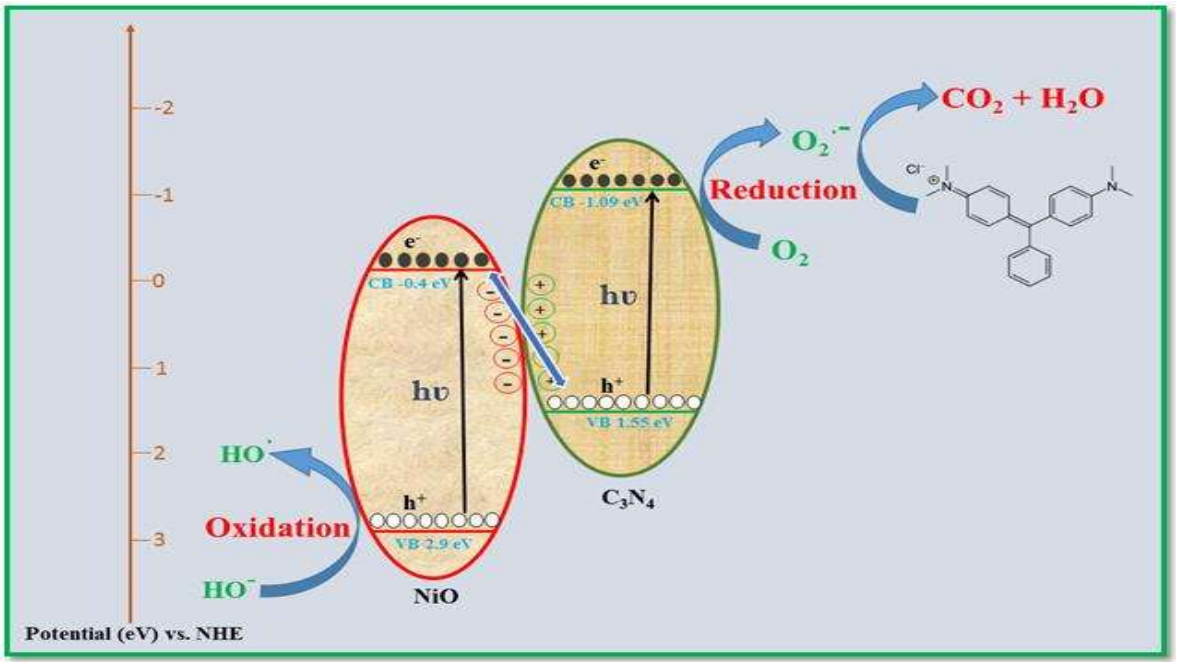

Fig. 3.11 Probable mechanism for the removal of MG by SK-3 under UV-light

In this work, a novel heterojunction nanocomposite following S-scheme was formed due to the interaction of chemical bonds between the interfaces of the nanocomposite. The electrons from the CB of NiO and holes from the VB of g-C_3N_4, which are relatively useless, are now recombined with each other due to the effect of the internal electric field and band bending interactions, while the useful electrons and holes in the CB of g-C_3N_4 and VB of NiO having

higher redox potential are retained. The electrons on the CB of g-C_3N_4 could reduce O_2 to $O_2^{\bullet-}$ and holes on the VB of NiO could oxidize OH^- to $OH^{\bullet}$, which are the major active species generated during the photocatalytic degradation experiment.

3.4.6.4 Turn over frequency (TOF) and recyclability

TOF of the SK-3 catalyst is calculated by using (Gomathi Devi et al., 2009; Zyoud et al., 2015).

$$\textbf{Turnover frequency} = \frac{\frac{\boldsymbol{Number\ of\ moles\ of\ reactant}}{\boldsymbol{Number\ of\ gram\ of\ catalyst}} \times \boldsymbol{Yield}}{\boldsymbol{time\ (min)}} \qquad (3.6)$$

The calculated TOF of SK-3 was compared with the TOF of other photocatalysts, which are used for the degradation of MG from different works of literature; the data is shown in Table 3.2. From the table, we can see that SK-3 has a much higher TOF than previously reported literature.

Table 3.2 Comparison table of TOF value obtained from MG degradation by various photocatalysts

S. No.	Photocatalysts	Source of illumination	TOF [mole $g^{-1}min^{-1}$]	Reference
1.	Mn/BiOCl	Halogen lamp (500 W)	7.99×10^{-7}	(Pare et al., 2011)
2.	ZnO (flower-like)	Mercury lamp (30 W)	1.05×10^{-5}	(Saikia et al., 2015)
3.	SnO_2/CuO	UV-Light (15 W)	2.92×10^{-6}	(Kumar et al., 2016)

4.	NiO0.8ZnO0.2/ZnO	UV lamp (18 W)	7.53×10^{-7}	(Milenova et al., n.d.)
5.	α-Fe_2O_3/SnO_2	Solar light	8.95×10^{-6}	(Pradhan et al., 2014)
6.	TiO_2/ZnO	UV-light (4×30 W)	1.11×10^{-6}	(Bansal et al., 2009)
7.	Pt/In_2O_3/CdS	Xenon lamp (300 W)	5.71×10^{-6}	(Qusti et al., 2018)
8.	CNT/ZnO	LED lamp (200 W)	1.08×10^{-5}	(Arsalani et al., 2020)
9.	Pt/ZnO	Xenon lamp (300 W)	1.83×10^{-5}	(Mohamed et al., 2016)
10.	NiO	UV- Laser	8.60×10^{-6}	(Hayat et al., 2011)
11.	NiO/GO	Mercury lamp (500 W)	5.82×10^{-6}	(Ahmad et al., 2018)
12.	WO_3/C_3N_4	Tungsten lamp (500 W)	3.79×10^{-6}	(J. Zhao et al., 2015)
13.	***g-C_3N_4/NiO (SK-3)***	***UV light (8 W)***	***2.21×10^{-5}***	***Present work***

To check the reusability and stability of the SK-3 photocatalyst, we performed the recyclability experiment and characterized the used photocatalyst through HR-XRD. The result of recyclability (figure 3.12a.) displays that the synthesized nanocomposite (SK-3)

catalyst degrades almost the same amount of MG up to the 3rd cycle, and only a 5% decrement was observed in 4th cycle. However the XRD pattern of the used photocatalyst (figure 3.12b) shows that, there are no significant changes is observed in the crystal structure and no any extra peaks or phase change was observed, which confirms the stability of the synthesized photocatalyst.

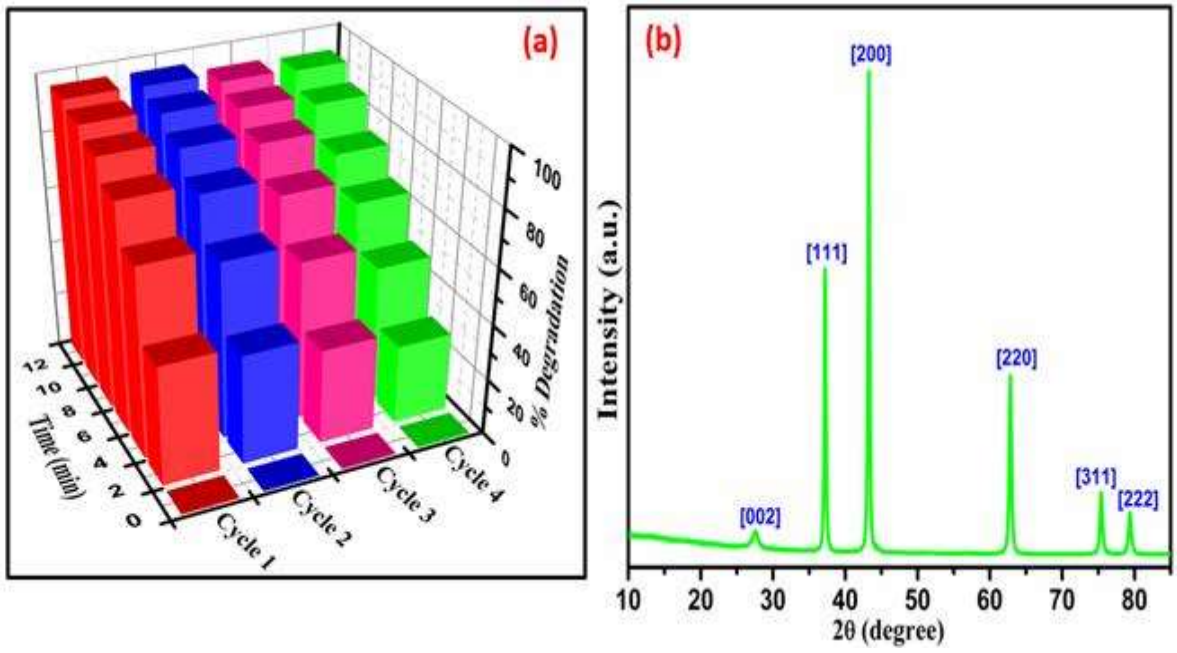

Fig. 3.12 (a) Recyclability of SK-3 photocatalyst, (b) HR-XRD pattern of SK-3 after recyclability

3.5 Conclusions

From the above results and discussion, we can conclude our work in the following points given below-

- Our synthesized catalyst is a mesoporous and hexagonal shape in the range of 25-35 nm, which is very close to the crystallite size.
- Higher rate of adsorption of dye on the surface of nanocomposite SK-3, because of larger surface area (22 m^2/g) and pore diameter (40-50 nm).
- g-C_3N_4 plays a vital role in the separation of the photogenerated excitons (e^-/h^+).

- A novel p-n junction formed between g-C_3N_4 and NiO, responsible for the higher photocatalytic activity of the SK-3 nanocomposite.
- The primary reactive species formed in the photocatalytic experiment is $O_2^{\bullet-}$ radical.
- For the mineralization of MG (2.76×10^{-5} mol/liter), the optimized amount of the catalyst (0.1 mg/mL) degrades 96% of the dye with good recyclability.
- The synthesized SK-3 nanocomposite has much higher TOF (2.21×10^{-5} mole $g^{-1}min^{-1}$) than other reported photocatalysts for MG degradation.
- Photocatalyst SK-3 is an efficient candidate for the mineralization of the pollutant without photocorrosion.